Gradient-enhanced damage growth modelling of ductile fracture

Received: 8 January 2021 | Revised: 24 May 2021 | Accepted: 14 June 2021

DOI: 10.1002/nme.6768

RESEARCH ARTICLE

WILEY

Gradient-enhanced damage growth modeling of ductile fracture

Ragnar Larsson | **Ahmet S. Ertürk**

Division of Material and Computational Mechanics, Department of Industrial and Materials Science, Chalmers University of Technology, Gothenburg, Sweden

Correspondence
Ragnar Larsson, Division of Material and Computational Mechanics, Department of Industrial and Materials Science, Chalmers University of Technology, Gothenburg, SE-412 96, Sweden.
Email: ragnar@chalmers.se

Abstract

We present a gradient-enhanced damage model for ductile fracture modeling, describing the degraded material response coupled to temperature. Continuum thermodynamics is used to represent components of the energy dissipation as induced by the effective material response, thermal effects, and damage evolution. The viscoplastic Johnson-Cook constitutive model serves as prototype for the effective material. The continuum damage evolution of Lemaitre type is focusing the degradation of the shear response, eventually leading to ductile shear failure. A novel feature is the damage-driving dissipation rate, allowing for elastic and plastic components separated by a global damage threshold for accumulation of inelastic damage-driving energy. In the application to a dynamic split-Hopkinson test and two quasi-static tensile tests, the gradient damage model is compared with the corresponding local model. For isothermal conditions, the examples show that both damage models exhibit mesh convergent behavior when using the global damage threshold.

KEYWORDS

continuum damage, damage-driving energy, ductile fracture, gradient damage, mesh convergence

1 | INTRODUCTION

Finite element modeling and simulation of machining processes relates strongly to the ability of the constitutive model to represent localized shear and chip form in the vicinity of the cutting tool.[1-3] These phenomena can be modeled using thermoviscoplasticity combined with continuum damage to describe ductile failure for the representation of serrated chip formation.[4] The major ductile failure scenario is that failure initiates with void nucleation/microcrack development that coalesce, first on the microstructural level, eventually forming a macroscopic crack or a diffuse damage zone on the macroscale. In many engineering fields, for example, machining and lightweight design, ductile failure is an important phenomenon to account for. It is of vital importance to efficiently and accurately control the fracture process. To achieve this, finite element based continuum damage modeling needs to correctly predict important features such as stress state, damage/initiation/propagation, load carrying capacity of the structure associated with the damage patterns.

From the key work of Gurson,[5] ductile damage is attributed to growth of microvoids, whose evolution is formulated in (local) Gurson-type plasticity models. Various formulations of the Gurson-based void growth have been considered, for existing and nucleated voids including the morphology of the voids, for example, Needleman and Tvergaard,[6] Pardoen and Hutchinson.[7] In the FE-application, the void formation is assumed to coalesce into fracture surfaces

corresponding to localized deformation that is highly mesh dependent for standard constitutive theories. As a remedy to the highly mesh-dependent behavior, nonlocal extensions of the Gurson model have been proposed.[8,9] Later developments in this direction are represented by the Rousselier model to monitor the void growth. A nonlocal enhancement of the volumetric plastic strain has been proposed to improve the mesh convergence.[10] Another way to represent ductile fracture is to generalize recent developments of continuum phase field models for brittle fracture processes, for example, References 11-14, to ductile fracture, for example, References 15,16.

In Miehe et al.,[16] the proposed phase field modeling is introduced into a thermoplasticity framework in conjunction with a nonlocal damage model. For inelastic materials, or large inelastic zones near a crack, nonlinear fracture mechanics has been used based on the extended finite element methodology,[17] combined with the cohesive zone concept.[18,19] Some references exploiting the cohesive zone concept in this way are References 20-23. It has been argued that viscous regularization of the continuum material model coupled to damage via viscoplasticity may remove the pathological mesh dependence.[24-26] Recent developments using the phase field approach to ductile fracture[15,16,27,28] also indicates removed mesh dependence, even for highly refined meshes. Ductile fracture may also be modeled by extending continuum phase field models for brittle fracture processes[11,13,14,29] so that ductile fracture characteristics are included.[15,16] A recent paper[30] proposes rate-dependent damage evolution for ductile fracture processes to overcome mesh dependence without gradient damage enhancement.

In this article, the Johnson-Cook (JC) constitutive model[31] is exploited to describe ductile fracture in combination with a *global* damage threshold for inelastic damage evolution. In relation to the developments in Reference 30, extensions are developed to include the effect of nonlocal (or gradient) damage and to exchange the local fracture model[32] into a global damage threshold. As main prototype for the effective material, the JC model is considered to account for deformation and strain rate hardening and temperature degrading effects. In the damage modeling, we are concerned with

1. The energy dissipation rate (involving elastic and inelastic components) describing supplied damage-driving dissipation to the damage induced fracture area production process.
2. The description of energy dissipation due to fracture area production. In this development, fracture area production due to "damage convection" and "damage nucleation" is considered in the evolution of the damage field, cf. Reference 33. In addition, a "gradient" fracture area production effect is obtained due to spatial growth of the damage field.
3. Due to the slow or even nonexisting finite element convergence of internal variables, a global damage threshold is proposed for the onset of inelastic damage evolution.

In this fashion, the model facilitates an enhanced control of the damage evolution and fracture energy dissipation. It has been shown that this model, without the additional gradient effect,[30,33] can partly remove the pathological mesh dependence and have a stable behavior. A major incentive of the present investigation is thus to consider the total model convergence and stability in the finite element application. The modeling framework is demonstrated through finite element analyses of a dynamic split-Hopkinson test and two quasi-static (isothermal) tensile tests, showing the convergence properties of the model.

2 | A DAMAGE MODEL FOR DUCTILE FRACTURE

This section summarizes key developments for a recently developed damage model for ductile fracture including effects of thermodynamics. As compared with Reference 30, an extension is made to include gradient damage evolution in the context of elastic-plastic damage-driving energy and a global damage threshold.

2.1 | Kinematics

In order to describe the thermomechanical coupling in the model, the kinematic relations are first established. To this end, consider particles, with position $\boldsymbol{X}$ in the reference configuration B_0, in motion with the nonlinear deformation $\boldsymbol{\varphi}[\boldsymbol{X}, t]$ from $\boldsymbol{X} \in B_0$ to positions $\boldsymbol{x} \in B$ in the current configuration. The deformation gradient is $\boldsymbol{F} = \boldsymbol{\varphi} \otimes \nabla_{\boldsymbol{X}}$, where $\nabla_{\boldsymbol{X}}$ is the material gradient operator and $J = \det[\boldsymbol{F}]$ is the volumetric deformation. Consider also the deformation gradient subdivided into an elastic component $\boldsymbol{F}_e$, a purely thermal volumetric component $\boldsymbol{J}_\theta$ and the irreversible inelastic part $\boldsymbol{F}_p$, forming the total deformation gradient multiplicatively as

$$\boldsymbol{F} = \overline{\boldsymbol{F}} \cdot \boldsymbol{F}_p \ \text{ with } \ \overline{\boldsymbol{F}} = J_\theta^{1/3} \boldsymbol{F}_e, \tag{1}$$

where $\boldsymbol{J}_\theta = \det[\boldsymbol{F}_\theta] = 1 + \alpha_\theta(\theta - \theta_0)$, α_θ is the coefficient of thermal expansion, $\theta > 0$ is the absolute temperature, θ_0 is a reference temperature. In Equation (1), the "bar" indicates that $\overline{\boldsymbol{F}}$ is the reversible deformation, including elastic mechanical and thermal components. It follows for volume preserving inelastic deformation that

$$\det[\boldsymbol{F}] = \boldsymbol{J} = \overline{\boldsymbol{J}} = \boldsymbol{J}_e \boldsymbol{J}_\theta \ \text{ with } \ \boldsymbol{J}_p := 1. \tag{2}$$

From the multiplicative split, an additive decomposition of the spatial velocity gradient $\boldsymbol{l} = \dot{\boldsymbol{F}} \cdot \boldsymbol{F}^{-1}$ is induced in recoverable and inelastic portions $\bar{\boldsymbol{l}}$ and $\boldsymbol{l}_p$ as

$$\boldsymbol{l} = \bar{\boldsymbol{l}} + \boldsymbol{l}_p \ \text{ with } \ \bar{\boldsymbol{l}} = \dot{\overline{\boldsymbol{F}}} \cdot \overline{\boldsymbol{F}}^{-1} \ \text{ and } \ \boldsymbol{l}_p = \boldsymbol{F}_e \cdot \boldsymbol{L}_p \cdot \boldsymbol{F}_e^{-1}, \tag{3}$$

where $\boldsymbol{L}_p := \dot{\boldsymbol{F}}_p \cdot \boldsymbol{F}_p^{-1}$ is the plastic velocity gradient. Related to the adopted *isotropic* viscoplasticity modeling, let us also introduce the symmetric plastic rate of deformation tensor as

$$\boldsymbol{d}_p = \boldsymbol{l}_p^{\text{sym}} = -\mathcal{L}_v[\overline{\boldsymbol{b}}] \cdot \overline{\boldsymbol{b}}^{-1} \ \text{ with } \ \mathcal{L}_v[\overline{\boldsymbol{b}}] = \frac{1}{2} \boldsymbol{F} \cdot \dot{\overline{\boldsymbol{F}^{-1} \cdot \overline{\boldsymbol{b}} \cdot \boldsymbol{F}^{-t}}} \cdot \boldsymbol{F}^t, \tag{4}$$

where $\mathcal{L}_v[\overline{\boldsymbol{b}}]$ is the Lie derivative in terms of the reversible Finger tensor $\overline{\boldsymbol{b}} = \overline{\boldsymbol{F}} \cdot \overline{\boldsymbol{F}}^t$.

2.2 | Damage degraded effective material

A damage model is outlined for ductile failure of Lemaitre type, where the effective material model is degraded by damage. The model is formulated so that the damage evolution is coupled to the stored free isochoric energy of the effective material, where we use the notation $\hat{\bullet}$ for the effective response. This is described by degrading the isochoric free energy in terms of the scalar damage variable $0 \leq \alpha \leq 1$ so that

$$\rho_0 \psi = f[\alpha] \rho_0 \hat{\psi}^{\text{iso}}[\overline{\boldsymbol{b}}^{\text{iso}}] + g[\theta] \rho_0 \hat{\psi}^{\text{mic}}[k] + \rho_0 \psi^{\text{vol}}[J, \theta] + \rho_0 \psi^{\text{th}}[\theta], \tag{5}$$

where $f[\alpha] = (1 - \alpha)^2$ is the degradation function, ρ_0 is the density in the reference configuration and $\hat{\psi}^{\text{iso}}$ is the effective isochoric stored free energy of elastic deformation contained in the isochoric Finger tensor $\overline{\boldsymbol{b}}^{\text{iso}} = \boldsymbol{b}_e^{\text{iso}}$. Hence, there is no temperature dependence in $\hat{\psi}^{\text{iso}}$. Moreover, $\hat{\psi}^{\text{mic}}$ represents stored energy due to internal (isotropic) hardening processes in the material (represented by the effective plastic strain k) and ψ^{th} is the thermal part describing stored free energy induced by the temperature θ. To more specific, the viscoplastic JC constitutive model[31] serves as the effective material response with the temperature degradation function $g[\theta]$ degrading the micro hardening in Equation (5) as

$$g[\theta] = \begin{cases} 1 & \theta \leq \theta_{\text{trans}} \\ 1 - \left(\frac{\theta - \theta_{\text{trans}}}{\theta_{\text{melt}} - \theta_{\text{trans}}} \right)^m & \theta_{\text{trans}} < \theta < \theta_{\text{melt}} \\ 0 & \theta \geq \theta_{\text{melt}} \end{cases}, \tag{6}$$

where m is the temperature degradation exponent, whereas θ_{trans} and θ_{melt} are room and melting temperatures, respectively.

In order to represent the effective shear and volumetric parts of the material response, the following explicit expressions are considered

$$\begin{aligned} \rho_0 \hat{\psi}^{\text{iso}} &= \frac{1}{2} G \left(\mathbf{1} : \overline{\boldsymbol{b}}^{\text{iso}} - 3 \right), \ \rho_0 \hat{\psi}^{\text{mic}} = \frac{B}{n+1} |k|^{n+1}, \\ \rho_0 \psi^{\text{vol}} &= \frac{1}{2} K \log[\boldsymbol{J}_e]^2 \approx \frac{1}{2} \boldsymbol{K} \log[\boldsymbol{J}]^2 - 3 \boldsymbol{K} \alpha_\theta (\theta - \theta_0) \log[\boldsymbol{J}]. \end{aligned} \tag{7}$$

Here, $\boldsymbol{G}$ is the shear modulus and ψ^{vol} is the stored free energy in the natural logarithm due to elastic volume change $\boldsymbol{J}_e$ with bulk modulus $\boldsymbol{K}$. The parameters related to the microhardening are the material hardening B and the hardening exponent n of the JC model. The constitutive relations are derived from the dissipation inequality

$$\mathcal{D} = \boldsymbol{\tau} : \boldsymbol{l} - \rho_0 \dot{\psi}_{|\theta} = f[\alpha]\hat{w}_p + \kappa \dot{k} + \mathcal{A}\dot{\alpha} \geq 0 \text{ with } \hat{w}_p = \hat{\boldsymbol{\tau}}^{\text{iso}} : \boldsymbol{d}_p \geq 0, \tag{8}$$

where $\mathcal{D}$ the mechanical dissipation rate, $\hat{w}_p$ is the plastic work rate of the *effective* material, and $\mathcal{A}$ is the elastic damage-driving energy contribution, cf. References 34 and 35. From the inequality in Equation (8), the constitutive equations for the isochoric effective Kirchhoff stress $\hat{\boldsymbol{\tau}}^{\text{iso}}$ and the microhardening stress κ are obtained as

$$\boldsymbol{\tau} = f[\alpha]\hat{\boldsymbol{\tau}}^{\text{iso}} - \boldsymbol{J}p\boldsymbol{1}, \; p = -\rho_0 \frac{\partial \psi^{\text{vol}}}{\partial \boldsymbol{J}}, \; \kappa = -g[\theta]\rho_0 \frac{\partial \psi^{\text{mic}}}{\partial k} = -g[\theta]\boldsymbol{B}|k|^n \text{ sign}[k], \tag{9a}$$

$$\hat{\boldsymbol{\tau}}^{\text{iso}} = 2\rho_0 \frac{\partial \hat{\psi}^{\text{iso}}}{\partial \overline{\boldsymbol{b}}} \cdot \overline{\boldsymbol{b}} = G\overline{\boldsymbol{b}}^{\text{iso}}_{dev}, \; \mathcal{A} = -f'[\alpha]\rho_0 \hat{\psi}^{\text{iso}}. \tag{9b}$$

Upon assuming adiabatic conditions, the energy equation associated with Equations (9)–(8) reads

$$c_v \dot{\theta} = f[\alpha]\hat{w}_p + \mathcal{A}\dot{\alpha} - 3K\alpha_\theta \theta \, \boldsymbol{1} : \boldsymbol{d} + \left(\kappa + \theta \frac{\partial \kappa}{\partial \theta}\right) \dot{k}, \tag{10}$$

where $c_v = -\rho_0 \theta \frac{\partial^2 \psi^{\text{th}}}{\partial \theta^2}$ is the specific heat capacity.

2.3 | Viscoplastic evolution rule

To ensure positive dissipation rate $\mathcal{D} \geq 0$ in Equation (8), it suffices to consider $\hat{w}_p \geq 0$, $\dot{\alpha} \geq 0$ and $\dot{k} \geq 0$ (since $\mathcal{A} > 0$ and $\kappa > 0$ always). Following the JC model, the static "von Mises" yield function is introduced as

$$\phi_s = \hat{\tau}_e - (g[\theta]A + \kappa), \; \hat{\tau}_e = \sqrt{\frac{3}{2}}|\hat{\boldsymbol{\tau}}^{\text{iso}}|, \tag{11}$$

where $\hat{\tau}_e$ is the von Mises stress of the effective stress response and A is the initial yield stress. Here it is assumed that g[θ] degrades the yield stress $A + \kappa$ in the same way as the effective hardening in Equation (5). To account for strain rate hardening effects according to the JC model, a rate-dependent yield function is formulated in terms of the quasi-static one as

$$\phi = \phi_s - (g[\theta]A + \kappa) \, C \log\left[\frac{\dot{\epsilon}}{\dot{\epsilon}_0}\right], \tag{12}$$

where C is a viscosity parameter, $\dot{\epsilon} \geq \dot{\epsilon}_0$ is the effective strain rate, cf. Equation (14) below, and $\dot{\epsilon}_0$ is the reference strain rate parameter.

The following viscoplastic flow rules are considered

$$\boldsymbol{d}_p = \lambda \frac{\partial \phi_s}{\partial \hat{\boldsymbol{\tau}}^{\text{iso}}} = \lambda \frac{3}{2} \frac{\hat{\boldsymbol{\tau}}^{\text{iso}}}{\hat{\tau}_e}, \; \dot{k} = \lambda \frac{\partial \phi_s}{\partial \kappa} = -\lambda \text{ with } \phi \leq 0, \; \lambda \geq 0, \; \phi\lambda = 0, \tag{13}$$

where the evolution rules were complemented by the Kuhn–Tucker conditions to distinguish elastic and plastic loading. In order to comply to these conditions, the evolution rules for $\boldsymbol{d}_p$ and $\dot{k}$ are governed by the JC-viscoplastic evolution rule

$$\dot{\epsilon} := \lambda = \dot{\epsilon}_0 \exp\left[\frac{1}{C} \frac{\langle \phi_s \rangle}{g[\theta]A + \kappa}\right] \geq \dot{\epsilon}_0 \geq 0, \tag{14}$$

where $\langle \bullet \rangle$ is the positive part function (or Macaulay brackets). We also choose $\dot{\epsilon} = \lambda \geq \dot{\epsilon}_0$. It may be noted that the reference strain parameter $\dot{\epsilon}_0$ is generally a quite small number; however, to handle situations with very slow loading rates $\lambda < \dot{\epsilon}_0$, we set $C = 0$ in Equation (12) corresponding to rate-independent response as done in Reference 35.

2.4 | Damage-driving force and global damage threshold

To describe the damage-driving force including elastic and inelastic deformations for ductile fracture, we consider the damage/plasticity coupling in Equation (8). Following Reference 30, the dissipation rate $\mathcal{D}$ is reformulated to include the combined effects of effective elastic stored free energy and plastic work in the damage production, whenever the damage threshold time t_f is has been approached. This is formulated as

$$\mathcal{D}[t] = \begin{cases} f[\alpha]\hat{w}_p + \kappa\dot{k} + \underbrace{\mathcal{A}}_{\mathcal{A}_T}\dot{\alpha} & 0 \le t \le t_f \\ \dot{f}[\alpha]\hat{W}_p + \kappa\dot{k} + \underbrace{(\mathcal{A}+\mathcal{B})}_{\mathcal{A}_T}\dot{\alpha} & t \ge t_f \end{cases}, \tag{15}$$

where the inelastic damage-driving contribution $\mathcal{B}$ is defined as

$$\mathcal{B} = -f'[\alpha]\hat{W}_p \ \text{ with } \ \hat{W}_p = \int_{t_f}^{t} \hat{w}_p \, dt. \tag{16}$$

It is emphasized that $\mathcal{B}$ reflects inelastic damage-drive in terms of the *total* plastic work $\hat{W}_p$, due to continuous plastic deformation in the effective material. Moreover, $\mathcal{A}_T = \mathcal{A} + \mathcal{B}$ is the total damage-driving energy acting on $\dot{\alpha}$ to generate damage dissipation.

For modeling flexibility, the accumulation for $\hat{W}_p$ initiates from the threshold time t_f as alluded to in Equation (15). It appears that local FE-convergence in internal variables is problematic, in particular, in conjunction with damage degradation. For this reason, to arrive in an expression for t_f that avoids strong mesh dependence, we propose to formulate the damage threshold in the homogenized (or nonlocal) plastic strain $\overline{k}[t]$ formulated as

$$\overline{k}[t_f] - k_f = 0 \ \text{ with } \ \overline{k}[t] = -\frac{1}{m[\overline{B}_0]}\int_{\overline{B}_0} k \, dB \ \text{ and } \ k = -\int_0^t \lambda \, dt \ \text{ with } \ \lambda \ge 0, \tag{17}$$

where $\overline{B}_0 \subset B_0$ is generally the suitable subregion of the considered solid and $m[\overline{B}_0]$ is the volume. In the present article we have chosen $\overline{B}_0 = B_0$. The threshold time is thus the time it takes to attain the homogenized failure strain k_f. Evidently, the threshold for the inelastic damage-driving energy $\mathcal{B}$ to start accumulate happens when the volume mean of the plastic strain in the solid reaches the critical value k^f. In practice, the threshold time t_f is taken from the "previous" time increment, so that if $k^f - \overline{k} \ge 0$ is signaled at time $t = {}^n t$ then all integration points considers $t \ge t_f$.

2.5 | A nonlocal damage evolution model

In order to formulate the damage evolution model, we consider the dissipated fracture energy by smearing out the fracture area in a localization zone of finite width governed by the internal length parameter l_c, as indicated in Figure 1. In line with, for example, Larsson et al.,[33] the global fracture area functional Γ_l defines the total fracture area through

$$\Gamma_l = \int_{B_0} \gamma dB \ \text{ with } \ \gamma := \int_0^{\alpha} \left(\frac{\alpha}{l_c} + \frac{\dot{\alpha}}{v^*} - l_c \Delta\alpha \right) d\alpha, \tag{18}$$

where γ is the fracture area density per unit internal length. Here, the fracture area density takes on values based on damage state, the production of damage $\dot{\alpha}$ and gradient damage $\Delta\alpha$, where the gradient dependence is described via the material gradient ∇_X, in turn defining the Laplacian $\Delta = \nabla_X \cdot \nabla_X$ in Equation (18). The parameters involved in the fracture area density are the internal length parameter l_c, describing the diffuse character of the fracture area, and the fracture area progression speed parameter v^*, controlling the damage evolution $\dot{\alpha}$. The consequent rate of change of the fracture area is

$$\dot{\Gamma}_l = \int_{B_0} \dot{\gamma} dB \ \text{ with } \ l_c\dot{\gamma} = \alpha\dot{\alpha} + \frac{l_c}{v^*}\dot{\alpha}^2 - l_c^2 \Delta\alpha\dot{\alpha}. \tag{19}$$

For illustration/interpretation purposes, the Laplacian term in Equation (19) is written as

$$-l_c^2\Delta\alpha\dot{\alpha} = -l_c\nabla_X\cdot(\dot{\alpha}l_c\nabla_X\alpha) + (l_c\nabla_X\dot{\alpha})\cdot(l_c\nabla_X\alpha) = l_c\nabla_X\cdot(\boldsymbol{H}\dot{\alpha}) + \boldsymbol{H}\cdot\dot{\boldsymbol{H}}, \tag{20}$$

where $\boldsymbol{H} := -l_c\nabla_X\alpha$ is the gradient damage vector and $\dot{\boldsymbol{H}} = -l_c\nabla_X\dot{\alpha}$ is the corresponding rate of change vector. As indicated in Figure 1, the nonlocal damage flux is thus the negative gradient of the damage field scaled by the internal length l_c. Upon assuming zero damage normal flux $\boldsymbol{N}\cdot\boldsymbol{H} = 0$ along the outer boundary S_0 of the solid we find that

$$\begin{aligned} l_c\dot{\Gamma}_l = l_c\int_{B_0}\dot{\gamma}\,dB = \\ l_c\int_{S_0}\boldsymbol{N}\cdot(\boldsymbol{H}\dot{\alpha})\,dS + \int_{B_0}\left(\alpha\dot{\alpha} + \frac{l_c}{v^*}\dot{\alpha}^2 + \boldsymbol{H}\cdot\dot{\boldsymbol{H}}\right)dB = \\ \int_{B_0}\left(\alpha\dot{\alpha} + \frac{l_c}{v^*}\dot{\alpha}^2 + \boldsymbol{H}\cdot\dot{\boldsymbol{H}}\right)dB, \end{aligned} \tag{21}$$

whereby the local fracture area evolution $\dot{\gamma}$ can be characterized as

$$\dot{\gamma} = \frac{1}{2l_c}\dot{\overline{(\alpha^2 + |\boldsymbol{H}|^2)}} + \frac{1}{v^*}\dot{\alpha}^2 \geq 0. \tag{22}$$

The interpretation is shown in Figure 1, considering schematic isolevels of the damage state and its evolution. From Equation (22), there are three mechanisms governing the fracture area evolution: the first two mechanisms, $\dot{\overline{\alpha\alpha}}/(2l_c)$ and the rate of change of the damage gradient length $\dot{\overline{\boldsymbol{H}\cdot\boldsymbol{H}}}/(2l_c)$, are due to growth (or convection) of existing damage, whereas the term $\dot{\alpha}^2/v^*$ represents damage nucleation, cf. Reference 30. As depicted in Figure 1, the nonlocal damage term promotes fracture area evolution for damage gradient increase in the sense that $\dot{\overline{\boldsymbol{H}\cdot\boldsymbol{H}}} > 0$; however, gradient damage decrease $\dot{\overline{\boldsymbol{H}\cdot\boldsymbol{H}}} < 0$ may also occur in the damage zone. Note also that rate-independent fracture area evolution is obtained when the damage progression speed parameter $v^* \to \infty$.[30,33] In this case the damage production $\dot{\alpha}$ has no time to develop, and the fracture area establishes instantaneously for a given load. In the modeling of the fracture surface propagation, the progression speed parameter v^* should be in the order of the crack propagation speed. In practice it suffices to choose v^* "significantly" larger than the applied loading rate, as discussed in Section 4.

A balance between produced energy dissipation rate, because of fracture area production $\dot{\gamma}$ in Equation (22) and supplied damage dissipation rate from the damage-driving energy in Equation (15), may be established as

$$\mathcal{G}_c\dot{\gamma} = \mathcal{A}_T\dot{\alpha} \rightsquigarrow \frac{1}{l_c}\frac{\mathcal{G}_c}{v^*}\left(v^*(\alpha - l_c\Delta\alpha) + l_c\dot{\alpha}\right)\dot{\alpha} = \mathcal{A}_T\dot{\alpha}, \tag{23}$$

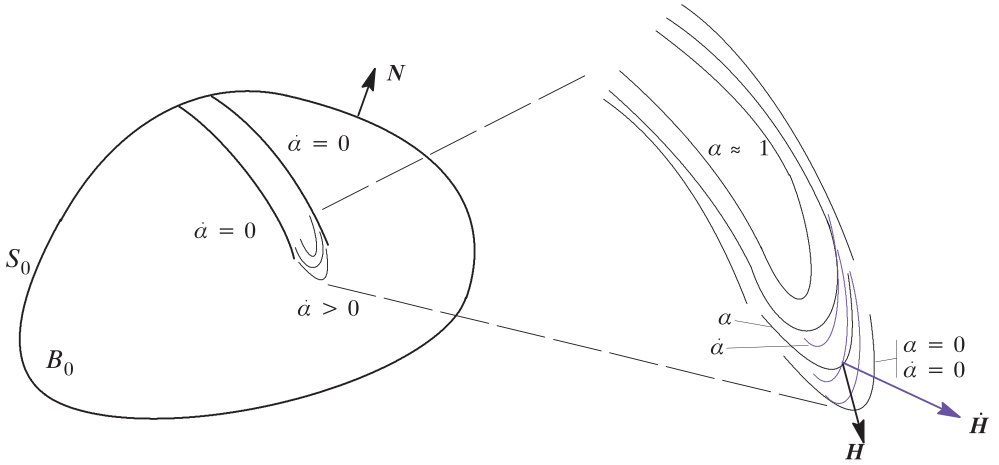

FIGURE 1 Localized damage progression zone in the solid region B_0 with external boundary S_0 and with unit normal $\boldsymbol{N}$. The close-up shows schematic isolines for the damage field (black) and the damage evolution field (magenta). The gradient damage vectors indicate damage gradient increase contribution to the fracture area

where $\mathcal{A}_T$ is the damage-driving energy in Equation (15), that becomes different depending on whether the damage threshold $t = t_f$ has been reached. In order to ensure the key condition $\dot{\alpha} \geq 0$, a dynamic damage loading function is introduced defined as

$$\phi_\alpha = \mathcal{A}_T - \frac{\mathcal{G}_c}{v^* l_c}\left(l_c\dot{\alpha} + v^*\left(\alpha - l_c^2\Delta\alpha\right)\right) \tag{24}$$

along with the loading conditions

$$\phi_\alpha \leq 0,\ \dot{\alpha} \geq 0,\ \phi_\alpha\ \dot{\alpha} = 0. \tag{25}$$

Respecting these damage loading conditions, we immediately obtain the damage evolution as the Bingham-type damage evolution law

$$l_c\dot{\alpha} = v^*\langle \alpha^s[\alpha] - \alpha + l_c^2\Delta\alpha\rangle \ \text{ with } \ \alpha^s = \frac{\mathcal{A}_T[\alpha]l_c}{\mathcal{G}_c}, \tag{26}$$

where $\langle\bullet\rangle$ is the positive part function (or McCauley bracket) and α^s represents the source of damage energy due to elastic and inelastic deformation.

3 | COUPLED WEAK FORMS FOR NONLOCAL DAMAGE EVOLUTION

In this section, the coupled problem between the displacement and damage fields due to nonlocal damage evolution is outlined. Please note that for the local damage model the damage field manifests as internal variables, which are directly linked to the stored free energy and the plastic work distributions via the damage-driving energy $\mathcal{A}_T$. For the globally coupled nonlocal problem, the primary fields representing diffuse damage evolution $\alpha[\boldsymbol{X}]$ and continuous displacement $\boldsymbol{u}[\boldsymbol{X}]$ are defined as

$$\{\boldsymbol{u} = \boldsymbol{u}[\boldsymbol{X}, t],\ \boldsymbol{F} = \boldsymbol{1} + \boldsymbol{u} \otimes \nabla_{\boldsymbol{X}}\} \in \mathcal{H},\ \{\alpha = \alpha[\boldsymbol{X}, t],\ \nabla_{\boldsymbol{X}}\alpha\} \in \mathcal{H}, \tag{27}$$

where $\mathcal{H}$ is the function space of square integrable gradient fields. Pertinent to the large deformation setting, the displacement field define the one to one Lagrangian mapping of a material point $\boldsymbol{X} \in \mathcal{B}_0$ to a material point in the deformed configuration $\boldsymbol{x} = \boldsymbol{\varphi}[\boldsymbol{X}] \in \mathcal{B}$, whereby it is required that the Jacobian $\boldsymbol{J} = \det[\boldsymbol{F}] > 0$.

3.1 | Weak forms

The weak form of the *quasi-static momentum balance* reads

$$\int_{\mathcal{B}_0} \boldsymbol{\tau} : (\boldsymbol{\nabla} \otimes \overline{\boldsymbol{u}})dB = \int_{\mathcal{B}_0} \rho_0\boldsymbol{b} \cdot \overline{\boldsymbol{u}}dB + \int_{\Gamma_0} \boldsymbol{t}_1 \cdot \overline{\boldsymbol{u}}dS\ \forall\overline{\boldsymbol{u}} \in \mathcal{H}, \tag{28}$$

where $\overline{\boldsymbol{u}}$ is the virtual displacement field.

In order to handle the damage loading conditions of Equation (26) numerically, let us introduce a regular nonlinear damage rate $(\dot{\alpha})^r$ upon introducing the negative part function $\langle\bullet\rangle_-$ to define

$$(\dot{\alpha})^r = \langle\dot{\alpha}\rangle + r^p\langle\dot{\alpha}\rangle_-, \tag{29}$$

where r^p is a penalization parameter. A regularized damage evolution rule is thus obtained from Equation (29) as

$$l_c(\dot{\alpha})^r = v^*\left(\alpha^s[\alpha] - \alpha + l_c^2\Delta\alpha\right). \tag{30}$$

The parameter r^p is chosen so that it penalizes the damage evolution $\dot{\alpha}$ in the damage unloading situation so that $\langle\dot{\alpha}\rangle_- \to 0$, whereas in damage loading we obtain the desired damage evolution.

Hence, the relation Equation (30) yields the weak form of the regularized nonlocal damage evolution problem as

$$\int_{\mathcal{B}_0} \left(\overline{\alpha}\, l_c(\dot{\alpha})^r + v^* \left(\overline{\alpha}\alpha + \overline{\boldsymbol{H}} \cdot \boldsymbol{H} \right) \right) dB = \int_{\mathcal{B}_0} \overline{\alpha}\, v^* \alpha^s[\alpha] dB \; \forall \overline{\alpha} \in \mathcal{H}, \tag{31}$$

where it was used (again) that $\boldsymbol{N} \cdot \boldsymbol{H} = 0$ along S_0 and $\overline{\boldsymbol{H}} = -l_c \nabla_X \overline{\alpha}$. Please note that the rate dependence in the present formulation is a key property to maintain control of the damage loading of the fracture area production via the penalization in Equation (30).

4 | NUMERICAL EXAMPLES

4.1 | Preliminaries

To observe the performance of the nonlocal and local versions of damage evolution in conjunction with the global damage threshold, three numerical examples are presented. Both gradient and local damage evolution are considered. The local rate dependent damage model is obtained by disregarding the Laplacian term in Equation (26). For this model, the damage field is an internal variable, integrated at the Gauss point level in terms of the damage-driving force of the effective stress–strain response. The FE-solutions are compared between the two damage models and the differences are observed.

The first example is a split-Hopkinson pressure bar test considering the dynamic properties of small grained size aged (SGA) INC718.[36] In this example the adiabatic thermal condition is assumed. A local iteration procedure is introduced so that the energy equation (Equation 10) is in balance with the produced plastic work rate. The second example is a quasi-static (isothermal) uniaxial tensile test of an I-shaped specimen considering a tensile test simulation of Al20204-T3.[15] The third example is a plane strain plate subjected to quasi-static tension in order to further highlight the convergence properties of the damage evolution laws.

As to nonlocal damage evolution, a staggered solution procedure is adopted during the time stepping to handle gradient damage. The staggering keeps the damage field fixed for each time step when solving the momentum balance in Equation (28), whereas the damage field is solved for a fixed configuration in Equation (31).[33] To maintain control of damage loading/unloading, the penalty parameter $r^p = 10$ in Equation (29) was found sufficient for the examples considered. In order to focus the postlocalized response, we set $\mathcal{A}_T = -f'[\alpha]\hat{W}_p$, thus neglecting the effect of elastic damage. Thereby, the prelocalized (inelastic) response of the specimens becomes identical for the different damage models up until the global damage threshold in Equation (17) has been approached. Bi-linear finite element discretization is used.

The hyperelastic-viscoplastic effective stress–strain response of the JC model has been implemented in FORTRAN, exploiting the multiplicative split of the deformation gradient into recoverable and inelastic portions along with the spatial format of the constitutive equations described in Section 2. This model is used in all three examples for the effective material response. The considered JC-parameters are given in Table 1.

The geometrical details of the split-Hopkinson pressure bar test is given in Figure 2(A). To reduce computational time, only the half of the geometry is simulated with the plane strain condition. Boundary conditions are introduced on the top edge (see Figure 2), where the specimen is compressed vertically with a prescribed velocity $\dot{u} = 1.5 \times 10^4$ mm/s. This value is chosen based on the observed global strain rate in Reference 36. Displacements are fixed at the bottom edge. The JC model is used with the parameters for the INC718 material in Table 1. Additional material properties common to both examples are given in Table 2.

The geometry of the specimen for the uniaxial tensile test can be seen in Figure 2(B). In this example, the specimen is constrained at the bottom edge, and the velocity is applied as a tensile load at the top edge with $\dot{u} = 1$ mm/s.

TABLE 1 Johnson-Cook material parameters for numerical examples

JC-parameters	A	B	C	n	m	$\dot{\epsilon}_0$	T_m	T_0
INC718 (SGA)[36]	1415	1018	0.0083	0.437	1.156	1	1000	25
AL2024-T3[37]	257.658	300	0.0149	0.3	1.499	1	600	25

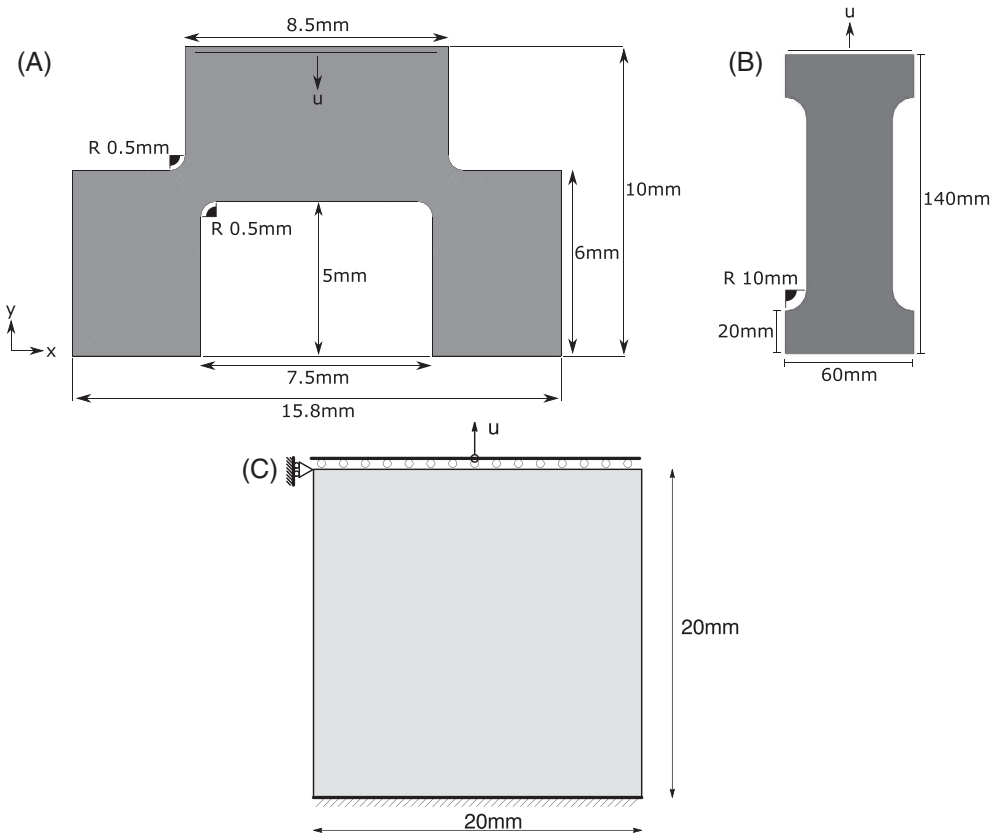

FIGURE 2 2D geometries of the specimens considered: (A) split-Hopkinson test (Example 1), (B) tensile specimen (Example 2), and (C) tensile loaded plane strain plate (Example 3)

TABLE 2 Material properties for numerical examples

Property (unit)	INC718	AL2024-T3
Elastic modulus (MPa)	185,000	72,400
Poisson's ratio (–)	0.33	0.33
Thermal expansion, m/(m °C)	1.3×10^{-5}	2.29×10^{-5}
Density (kg/m^3)	8190	2770
Specific heat, J/(kg °C)	435	875
Fracture energy (MPa mm)	77.7	9.31

Again, the JC model is used with parameters for the aluminum material in Table 1. In the third example, the plate in Figure 2(C) is clamped at the base and prevented to move horizontally at the top. The prescribed velocity is $\dot{u} = 1$ mm/s. Like in the split-Hopkinson test, the plate is assumed to be INC718. The parameters used are shown in Tables 1 and 2.

4.2 | Calibration of damage parameters

There are three damage related parameters in the model that need to be calibrated. These are k_f, v^*, and l_c. The fracture energy $\mathcal{G}_c$ is calculated based on data given in Reference 38 for the first example and taken from Reference 15 for the second example. This calibration is performed based on the reference data given in References 15,36. First of all, the damage threshold strain k_f is calibrated with respect to failure initiation. The selected values for the failure strain k_f are

shown in Table 3. After that, the damage progression speed parameter v^* is calibrated with respect to the rate dependence in the damage fracture area production. A too small value of v^* yields too much ductility in the response, whereas a too high value leads to unstable static damage evolution.[30] To choose the optimal v^*, our experience is that it should be chosen larger than the applied displacement rate $\dot{u}$. Hence, it is selected as $v^* = 10^7$ mm/s $\gg \dot{u} = 1.5 \times 10^4$ mm/s for the split-Hopkinson test, whereas for the tensile test in the second example the value of v^* can be reduced to $v^* = 10^3$ mm/s $\gg \dot{u} = 1$ mm/s. The internal length parameter l_c affects the width of the localization zone and the reaction force versus prescribed displacement relation in the postlocalized regime. This parameter is determined based on the data in References 15,36 to get the similar slope of the force drop in these references. The calibration process yields the l_c parameters given in Table 3 for the examples.

4.3 | Split-Hopkinson pressure bar specimen

Finite element plane strain simulation results of the split-Hopkinson pressure bar test are shown in Figure 3, in terms of reaction force versus prescribed compressive displacement curves. Five different meshes, with element sizes ranging from 0.012 to 0.2 mm, are used to evaluate the mesh sensitivity of the local and nonlocal damage evolution rules using a *local* threshold $k[t_f] = k_f$ (established at the Gauss point level). This local condition will be compared with the global damage threshold introduced in Section 2.4. As shown in Figure 3, the finite element solution of the demanding split-Hopkinson test does not converge for any of the considered damage models when using the local damage threshold. This is caused by the localized deformation in a narrow zone, see Figure 5, where the local plastic strain k does not seem to have any FE convergence property. Hence, we find that the local damage threshold can only be calibrated with respect to a selected mesh size, which in turn has to be quite fine to properly represent the localization zone realistically.

In order to resolve the problematic mesh sensitivity due to the local damage threshold, we advocate the global damage threshold proposed in Equation (17). When comparing Figures 3 and 4, significant influence of the thermal softening is obtained for refined meshes. For the finest mesh a degrading thermal effect is obtained, even prior to the onset of damage, thus reflecting the challenge to handle combined effects of thermal softening and damage. However, for the global damage threshold, the damage onset points along the curves in Figure 4(A,B) converges with refined meshes at the

TABLE 3 Calibrated damage parameters for the split-Hopkinson bar and the tensile test

Test/material	l_c (mm)	v^* (mm/s)	Local k_f (–)	Global k_f (–)
Split-Hopkinson pressure bar test/INC718 SGA	0.15	1×10^7	0.27	0.011
I-shaped specimen tensile test/Al20204-T3	0.90	1×10^3	–	0.0345
Plane strain plate/INC718 SGA	0.20	200	–	0.01

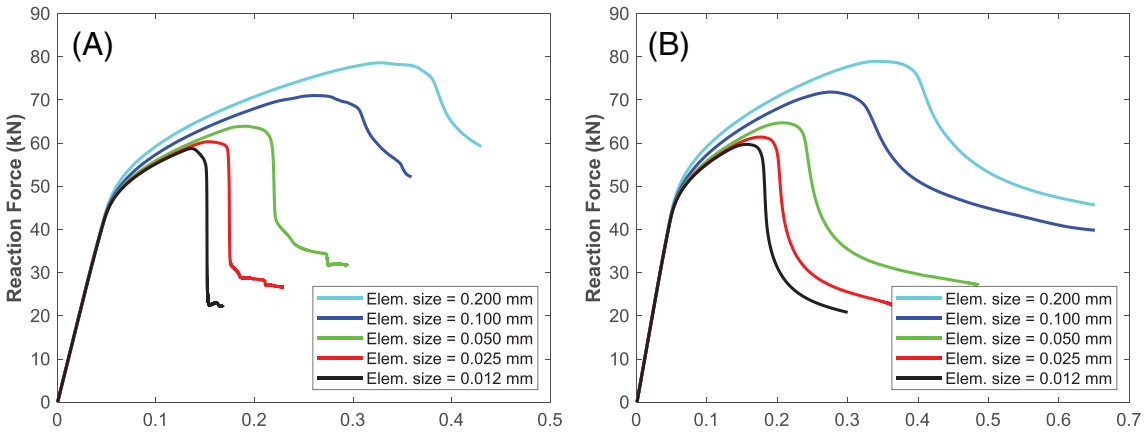

FIGURE 3 Reaction force versus prescribed displacement relations for the split-Hopkinson test using a *local* damage threshold. Mesh sensitivities using (A) the local damage model and (B) the nonlocal damage model

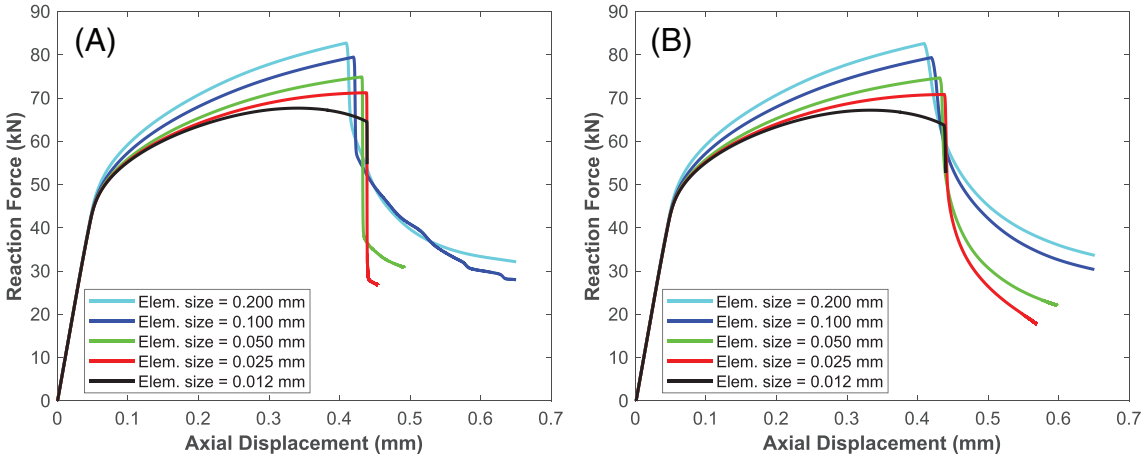

FIGURE 4 Reaction force versus prescribed displacement relations for the split-Hopkinson test using the *global* damage threshold Equation (17). Mesh sensitivities using (A) the local damage model and (B) the nonlocal damage model

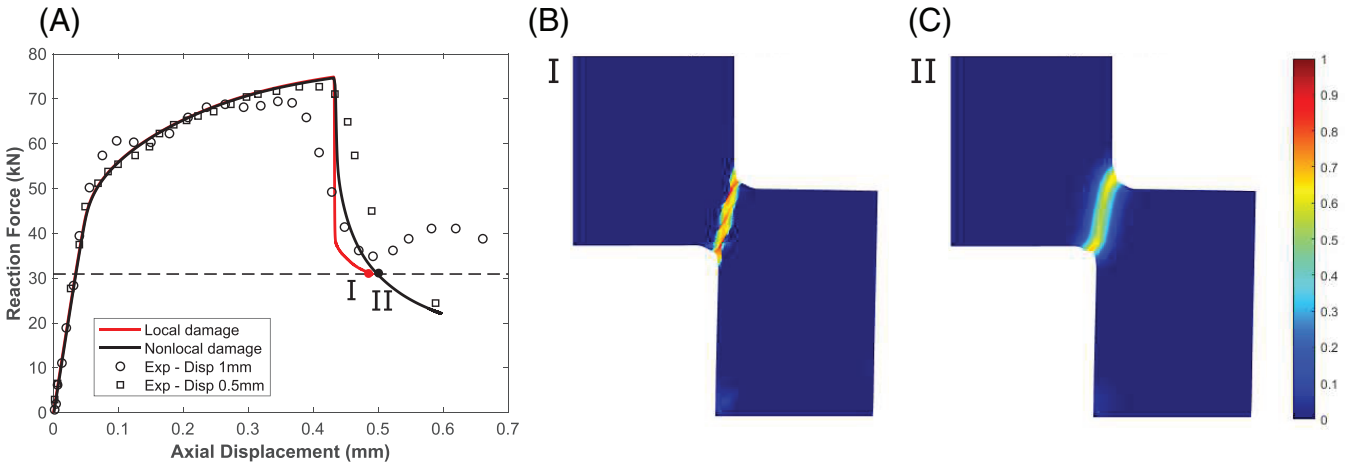

FIGURE 5 Comparison of local and nonlocal damage models for the mesh size 0.050 mm. (A) Reaction force versus prescribed displacement alongside experimental data[36] and (B, C) localized damage distributions $\alpha[\boldsymbol{X}]$ for the local and the nonlocal damage models

axial displacement ≈0.44 mm. By using the global damage threshold, the plastic strain is the volume mean of the specimen instead of the local plastic straining in the narrow deformation region. In this way, the calibration of the threshold strain k_f is much easier. The value for k_f can be decided based on the coarse mesh and then adjusted a little bit from the response of the finer meshes. For the rest of the article, the global damage threshold is used.

The comparison of the local and nonlocal damage models is presented in Figure 5, when using the intermediate element size 0.05 mm. In the figure, the force–displacement curves are given for both models as well as experimental data from Reference 36. It appears that both models behave in a similar fashion, with abrupt failure occurring as the damage threshold is approached. A slightly more regular softening behavior is obtained for the nonlocal damage model. On the right side of the figure, the damage distributions are given for both models with the same reaction force (at the points I and II along the curves in Figure 5). It can be seen that the local damage model results in strong shear localization ($\alpha \approx 1$) in the top and bottom regions of the narrow damage zone. This is in agreement with the corresponding experimentally observed macroscopic shear cracks in Reference 36. The nonlocal model yields a more distributed damage field around the same region. Figure 6 shows the temperature distribution at adiabatic conditions for the local and nonlocal damage models when using the same mesh size as in Figure 5. It is noted that the highest temperatures, ca 300°–350°, occur at the top edges of the shear zone. As expected, the nonlocal model yields a slightly higher temperature increase because of the consequent more energy consuming behavior in the postpeak regime.

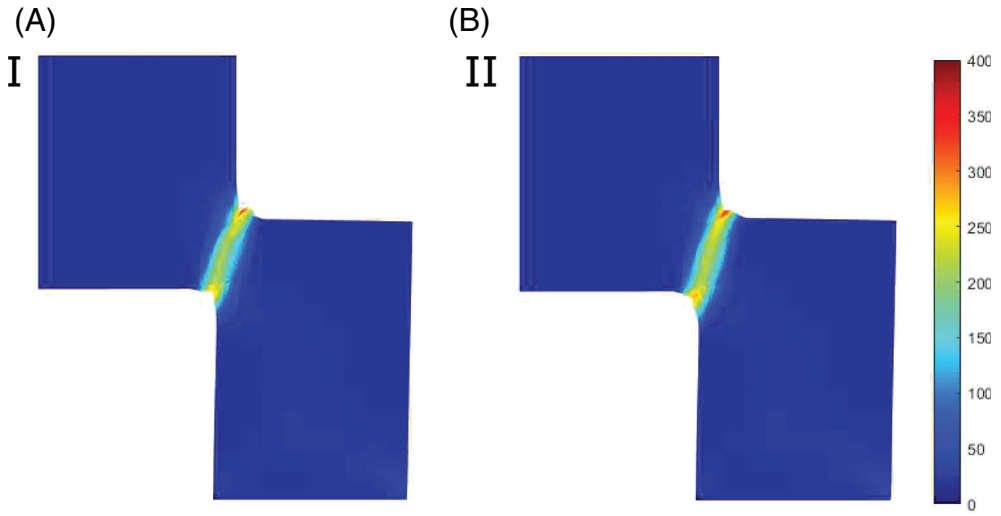

FIGURE 6 Comparison of local and nonlocal damage models for the mesh size 0.075 mm. (A, B) Temperature (°C) distributions for the local and the nonlocal damage models

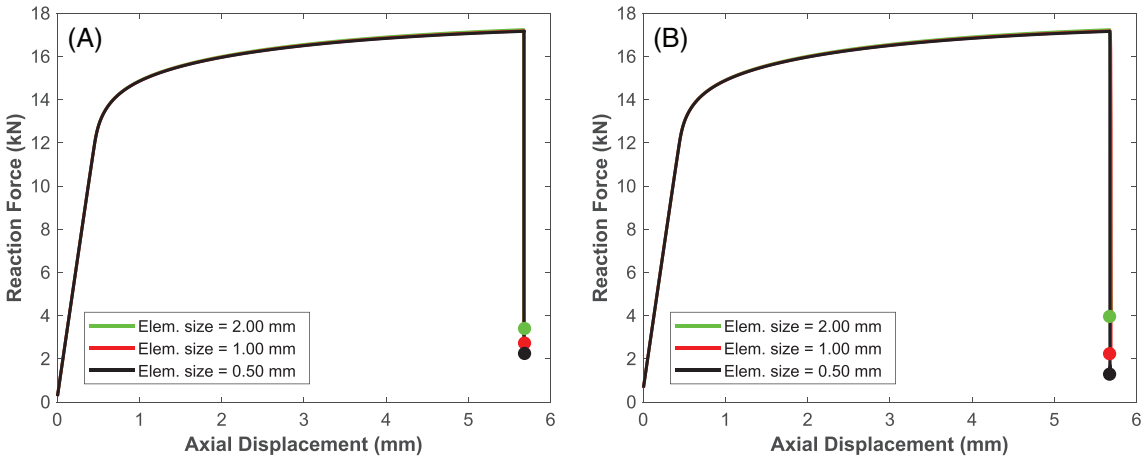

FIGURE 7 Reaction force versus prescribed displacement relations for the tensile test. The *global* damage threshold is used. Mesh sensitivities using (A) the local damage model and (B) the nonlocal damage model

4.4 | Uniaxial tensile test of I-shaped specimen

Mesh convergence results of the quasi-static uniaxial tensile test of the I-shaped specimen in Figure 2(B) are given in Figure 7. Three different mesh sizes are used, ranging from 0.5 to 2 mm for the finest to the crudest meshes. The global damage threshold is $k_f = 0.0345$. As shown in Figure 7, abrupt damage induced failure occurs starting from the damage onset point, corresponding to intense damage evolution and shear localization. To avoid convergence troubles in the end of the damage process, the analyses were stopped when the damage fields changed insignificantly. Since all curves are on top of each other, the results show that both models yield the same global behavior for all meshes considered. Indeed, mesh convergence is obtained with respect to the global damage onset condition. In line with Reference 15, the same abrupt decay of the reaction force is obtained for both damage models.

The results shown in Figure 8 are the calibrated results for the local and the nonlocal damage models with the reference data in Reference 15. The mesh size is 1.0 mm in the figure. Despite that the same reaction forces versus displacement response is obtained for both damage models, the damage pattern for the local damage model contains one distinct shear zone, whereas the nonlocal model exhibits a shear zone established after the decay of a competing localization zone. The obtained localized shear modes are in-line with the results for the ductile fracture model in Reference 15.

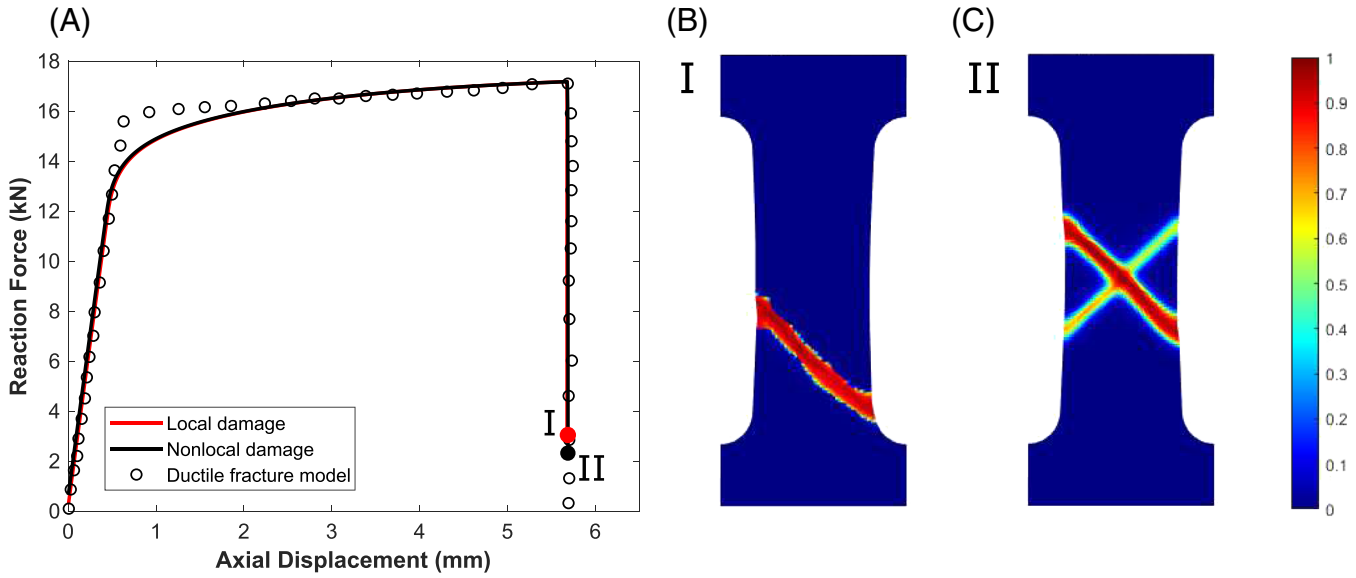

FIGURE 8 Comparison of local and nonlocal damage models for the mesh size 1.0 mm. (A) Reaction force versus prescribed displacement alongside ductile fracture model data from Reference 15 and (B, C) localized damage distributions $\alpha[\boldsymbol{X}]$ for the local and the nonlocal damage models

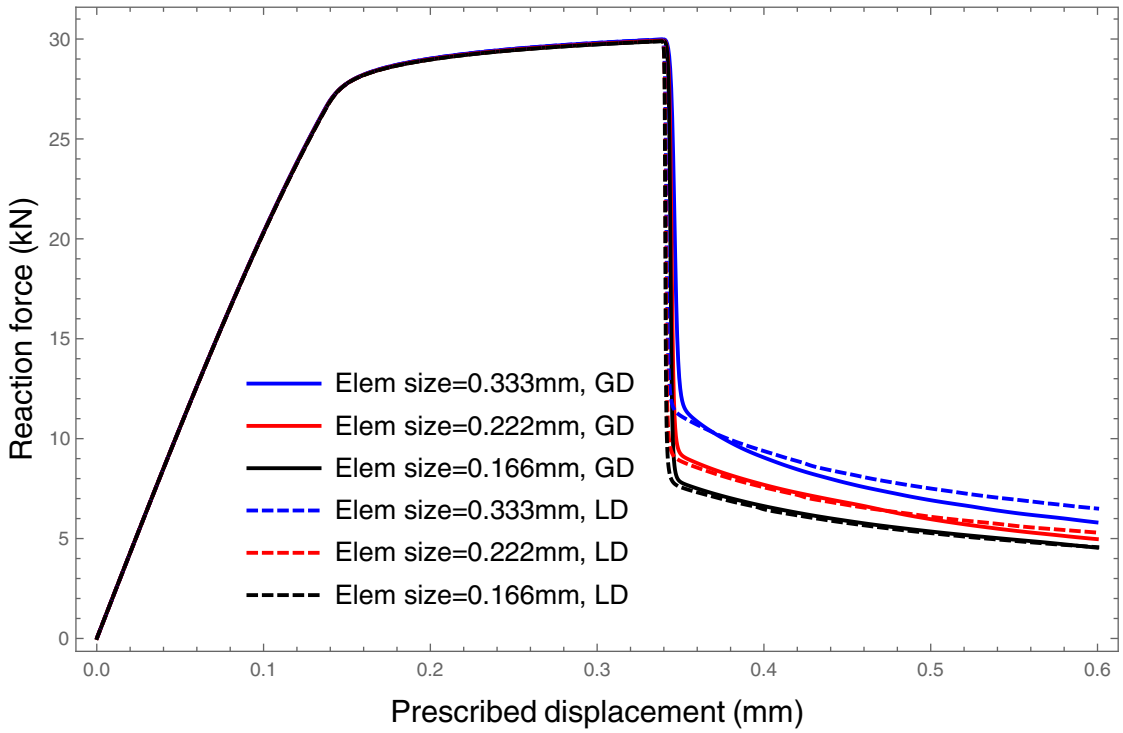

FIGURE 9 Reaction force versus prescribed displacement relations for element sizes 0.166, 0.222, and 0.333 mm. The analyses were made using the gradient damage (GD solid lines) and local damage (LD dotted lines) models

4.5 | Plane strain plate in tension

A plane strain plate is subjected to tensile prescribed displacement rate $\dot{u} = 1$ mm/s up to the total displacement $u = 0.6$ mm, as shown in Figure 2(C). As to damage in this example, the fracture energy is set to $\mathcal{G}_c = 24$ N/mm, while the remaining damage parameters are shown in Table 3.

Again, mesh convergence is studied. Since the loading rate is relatively small, the complication with thermal softening can be neglected. Three different meshes are considered for both the local and the gradient damage models. Structured meshing is adopted with meshes ranging from fine to crude bilinear element resolution, with the element

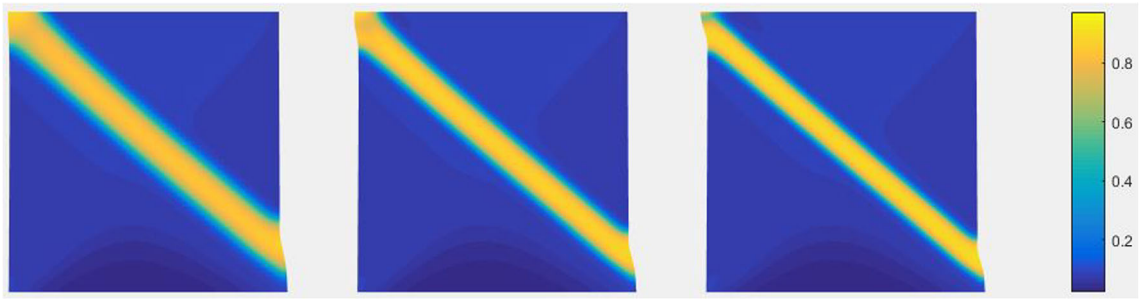

FIGURE 10 Damage distributions for crude to fine meshes at the final load step $r = 0.6$ mm: local damage model (LD)

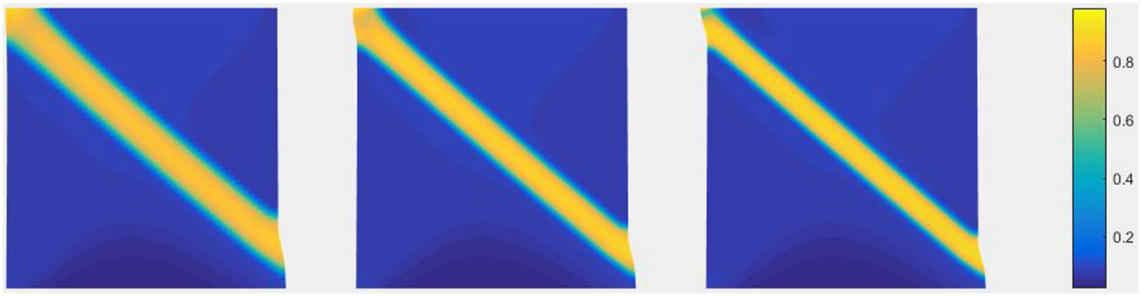

FIGURE 11 Damage distributions for crude to fine meshes at the final load step $r = 0.6$ mm: gradient damage model (GD)

sizes 0.333–0.166 mm. Figure 9 shows the mesh convergence in terms of reaction force versus prescribed displacement curves, considered to be the representative convergence measure of the entire loading process. It is noted that both models exhibit similar convergence behavior as the structured meshing of the 2D domain is refined. Governed by the effective JC material, almost identical response is obtained for all FE resolutions up to the failure point, which is well described by the global onset condition. After the drop from the peak load, the residual (crush) load is established at different levels depending on the mesh resolution. We note that the difference in crush load is reduced as the mesh is refined, indicating mesh convergence. Here it may be noticed that the gradient damage model (solid lines in Figure 9) seems to yield a slightly larger convergence rate compared with the local damage model. These results are complemented by the localized shear damage modes, successively converging into the same shear mode with increased element resolution in Figure 10 for the local damage model and in Figure 11 for the gradient damage model.

5 | CONCLUDING REMARKS

We have presented a gradient damage enhanced model for ductile fracture coupled to temperature. Continuum thermodynamics is used to describe the adopted damage/plasticity coupling. As prototype for the effective material, the viscoplastic JC-constitutive model was considered. A novel feature of the ductile damage model is the damage-driving dissipation rate, involving elastic and inelastic contributions separated by a *global* threshold for accumulation of inelastic damage-driving energy. From the balance between supplied and produced dissipation rate, the final damage model is obtained in terms of the diffuse fracture area parameters v^* and l_c. For comparison, the local rate dependent damage model in Reference 30 without the gradient damage term was considered. From the simulations, we conclude that the local threshold for inelastic damage-driving energy leads to a problematic mesh dependence of the finite element solution. The reason is that the plastic strain does not exhibit finite element convergence for mesh refinements. This fact was evidenced by the demanding split-Hopkinson test with strongly localized deformation in the shear failure zone, requiring very fine meshes to properly represent the behavior. As a remedy, when the effective material response is determined by the JC model, the global damage threshold seems to yield mesh convergent behavior up to damage initiation. Here, the split-Hopkinson case is more complex due to the dynamic material behavior in conjunction with the combined effects of thermal softening and damage. In the postlocalized regime, we find that the isothermal quasi-static second and third examples yield mesh convergent results for both the local and the nonlocal damage models. Implementationwise, the local damage model is amenable for implementation in commercial platforms like ABAQUS™. Challenges remain for how to implement nonlocal damage and the global damage threshold in other platforms than in-house.

ACKNOWLEDGMENTS

This research was financially supported by the Swedish national research program Vinnova-FFI (Strategic Vehicle Research and Innovation), project no. 2016-05397. The authors would also like to acknowledge the financial support of the Chalmers Area of Advance Production. The computations were performed on resources provided by the Swedish National Infrastructure for Computing (SNIC) at Chalmers Centre for Computational Science and Engineering (C3SE).

DATA AVAILABILITY STATEMENT

The data that support the findings of this study are available from the corresponding author upon reasonable request.

ORCID

Ragnar Larsson https://orcid.org/0000-0001-7593-8499

REFERENCES

1. Tay A, Stevenson M, de Vahl Davis G. Using the finite element method to determine temperature distributions in orthogonal machining. *Proc Inst Mech Eng*. 1974;188(1):627-638.
2. Arrazola P, Ozel T, Umbrello D, Davies M, Jawahir I. Recent advances in modelling of metal machining processes. *CIRP Ann Manuf Technol*. 2013;62:695-718.
3. Ljustina G, Larsson R, Fagerström M. A FE based machining simulation methodology accounting for cast iron microstructure. *Finite Elements Anal Des*. 2014;80:1-10.
4. FE modeling and simulation of machining Alloy 718 based on ductile continuum damage. *International Journal of Mechanical Sciences*. 2020;171:105375. http://dx.doi.org/10.1016/j.ijmecsci.2019.105375.
5. Gurson AL. Continuum theory of ductile rupture by void nucleation and growth: Part I - yield criteria and flow rules for porous ductile media. *J Eng Mater Technol*. 1977;99(1):14.
6. Tvergaard V, Needleman A. Analysis of the cup-cone fracture in a round tensile bar. *Acta Metall*. 1984;32(1):157-169.
7. Pardoen T, Hutchinson JW. An extended model for void growth and coalescence. *J Mech Phys Solids*. 2000;48:2467-2512.
8. Tvergaard V, Needleman A. Nonlocal effects on localization in a void-sheet. *Int J Solids Struct*. 1997;34(18):2221-2238.
9. Reusch F, Svendsen B, Klingbeil D. Local and non-local Gurson-based ductile damage and failure modelling at large deformation. *Eur J Mech A/Solids*. 2003;22:779-792.
10. Xu Y, Poh LH. Localizing gradient-enhanced Rousselier model for ductile fracture. *Int J Numer Methods Eng*. 2019;119:826-851. https://doi.org/10.1002/nme.6074
11. Miehe C, Welschinger F, Hofacker M. Thermodynamically consistent phase-field models of fracture: variational principles and multi-field FE implementations. *Int J Numer Methods Eng*. 2010;83:1273-1311.
12. Abiri O, Lindgren L. Non-local damage models in manufacturing simulations. *Eur J Mech A/Solids*. 2015;49:548-560.
13. Ambati M, Gerasimov T, De Lorenzis L. A review on phase-field models of brittle fracture and a new fast hybrid formulation. *Comput Mech*. 2014;55(2):383-405.
14. Miehe C, Schanzel LM, Ulmer H. Phase field modeling of fracture in multi-physics problems. Part I. balance of crack surface and failure criteria for brittle crack propagation in thermo-elastic solids. *Comput Methods Appl Mech Eng*. 2015;294:449-485.
15. Ambati M, Gerasimov T, De Lorenzis L. Phase-field modeling of ductile fracture. *Comput Mech*. 2015;55(5):1017-1040. https://doi.org/10.1007/s00466-015-1151-4
16. Miehe C, Hofacker M, Schanzel L, Aldakheel F. Phase field modeling of fracture in multi-physics problems. Part II. coupled brittle-to-ductile failure criteria and crack propagation in thermo-elastic-plastic solids. *Comput Methods Appl Mech Eng*. 2015;294:486-522.
17. Belytschko T, Black T. Elastic crack growth in finite elements with minimal remeshing. *Int J Numer Methods Eng*. 1999;45:601-620.
18. Dugdale DS. Yielding of steel sheets containing slits. *J Mech Phys Solids*. 1960;8:100-104.
19. Barenblatt GI. Mathematical theory of equilibrium cracks in brittle fracture. *Adv Appl Mech*. 1962;7:55-129.
20. Larsson R, Fagerström M. A framework for fracture modelling based on the material forces concept with XFEM kinematics. *Int J Numer Methods Eng*. 2005;62(13):1763-1788.
21. Fagerström M, Larsson R. Theory and numerics for finite deformation fracture modelling using strong discontinuities. *Int J Numer Methods Eng*. 2006;66:911-948.
22. Fagerström M, Larsson R. A thermo-mechanical cohesive zone formulation for ductile fracture. *J Mech Phys Solids*. 2006;56:3037-3058.
23. Mostofizadeh S, Fagerström M, Larsson R. XFEM-based element subscale refinement for detailed representation of crack propagation in large-scale analyses. *Int J Numer Methods Eng*. 2017;110:549-572.
24. Dias da Silva V. A simple model for viscous regularization of elasto-plastic constitutive laws with softening. *Commun Numer Methods Eng*. 2004;29:547-568.
25. Geers M, Brekelmans W, De Borst R. Viscous regularization of strain-localization for damage materials. *DIANA Computational Mechanics '94*. Dordrecht, Netherlands: Springer; 1994:127-138.
26. Niazi M, Wisselink H, Meinders T. Viscoplastic regularization of local damage models: revisited. *Comput Mech*. 2013;51(2):203-216.
27. Hofacker M, Miehe C. A phase field model for ductile to brittle failure mode transition. *Proc Appl Math Mech*. 2012;12:173-174.

28. Ulmer H, Hofacker M, Miehe C. Phase field modeling of brittle and ductile fracture. *Proc Appl Math Mech*. 2013;13:533-536.
29. Bourdin B, Francfort GA, Marigo JJ. Numerical experiments in revisited brittle fracture. *J Mech Phys Solids*. 2000;48(4):797-826.
30. A ductile fracture model based on continuum thermodynamics and damage. *Mechanics of Materials*. 2019;139:103197. http://dx.doi.org/10.1016/j.mechmat.2019.103197.
31. Johnson G, Cook W. A constitutive model and data for metals subjected to large strains, high strain rates and high temperatures. Paper presented at: Proceedings 7th International Symposium on Ballistics; April 19–21, 1983; Hague, Netherlands
32. Johnson G, Cook W. Fracture characteristics of three metals subjected to various strains, strain rates, temperatures and pressures. *Eng Fract Mech*. 1985;21:31-48.
33. Larsson R, Gutkin R, Rouhi S. Damage growth and strain localization in compressive loaded fiber reinforced composites. *Mech Mater*. 2018;127:77-90.
34. Larsson R, Razanica S, Josefson BL. Mesh objective continuum damage models for ductile fracture. *Int J Numer Methods Eng*. 2015;106:840-860.
35. Ljustina G, Fagerström M, Larsson R. Hypo and hyperinelasticity applied to modeling of compact graphite iron machining simulations. *Eur J Mech A/Solids*. 2012;37:57-68.
36. Johansson J, Persson C, Testa G, Ruggiero A, Bonora N, Hörnqvist CM. Effect of microstructure on dynamic shear localisation in Alloy 718. *Mech Mater*. 2017;109:88-100. https://doi.org/10.1016/j.mechmat.2017.03.020
37. Daoud M, Chatelain JF, Bouzid H. On the effect of Johnson cook material constants to simulate Al2024-T3 machining using finite element modeling. Volume 2A:Advanced Manufacturing, ASME 2014 International Mechanical Engineering Congress and Exposition 2014. American Society of Mechanical Engineers Digital Collection, 2014; Montreal, Quebec, Canada. https://doi.org/10.1115/IMECE2014-37170
38. Loria EA. *Superalloy 718 - Metallurgy and Applications*. Warrendale, PA: The Minerals, Metals and Materials Society; 1989.

How to cite this article: Larsson R, Ertürk AS. Gradient-enhanced damage growth modeling of ductile fracture. *Int J Numer Methods Eng*. 2021;1–16. https://doi.org/10.1002/nme.6768